High-Resolution FBG Strain Sensing With Dual-Comb Interrogation and Optimized Signal Processing

Malhar A. Nagar , *Graduate Student Member, IEEE*, Minghao Wei, *Graduate Student Member, IEEE*, Conor McArdle, Aleksandra Kaszubowska-Anandarajah, *Senior Member, IEEE*, Prince M. Anandarajah, *Senior Member, IEEE*, and Davide Janner.

Abstract—In this work, we present a high-resolution strain sensing system based on Dual Optical Frequency Comb (DOFC) interrogation of Fiber Bragg Gratings (FBGs), employing optimized signal processing methods for both reflection and transmission spectra. Femtosecond (fs) written FBGs with non-uniform profiles with bandwidths of ~ 0.5 nm were interrogated using a mutually coherent DOFC generated by externally injected gain-switched lasers (EI-GSLs). Different algorithms were used to process the DOFC signal to extract the FBG frequency shifts caused by the various strain increments. Using these approaches, we could detect strains with a sub- $\mu\varepsilon$ resolution (0.32 $\mu\varepsilon$), sensitivities ranging from 0.7–1 pm/ $\mu\varepsilon$, and a dynamic range of 422 $\mu\varepsilon$. These methods increased low-strain sensitivity typical of DOFC interrogation systems, enabling precise monitoring of standard off-the-shelf fswritten FBGs. The DOFC system showed enhanced linearity (R² \sim 0.98) and Figure of Merit (FoM - 2.58/ $\mu\varepsilon$) at lower strains than a standard commercial interrogator ($R^2 \sim 0.82$ and FoM – $0.88/\mu\varepsilon$). Our findings highlight the potential of the DOFC-FBG interrogation as a powerful tool for real-time high-resolution sensing applications, ranging from structural health monitoring to biomedical diagnostics.

Index Terms—Dual optical frequency comb (DOFC), externally injected gain-switched lasers (EL-GSLs), fiber Bragg gratings (FBGs), high-resolution strain sensing, signal processing, static strain sensing.

Received 19 February 2025; revised 23 April 2025; accepted 26 April 2025. Date of publication 9 May 2025; date of current version 4 August 2025. This work was supported in part by European Unions Horizon 2020 Research and Innovation Programme through the Marie Sklodowska-Curie under Grant 860185, in part by PHAST-ITN Project, in part by ICON Project under Grant 101189703, and in part by the NATO Science for Peace and Security under Project G6056. (Corresponding authors: Davide Janner; Prince M. Anandarajah.)

Malhar A. Nagar and Davide Janner are with the Dipartimento di Scienza Applicata e Tecnologia (DISAT), Politecnico di Torino, 10129 Turin, Italy (e-mail: malhar.nagar@polito.it; davide.janner@polito.it).

Minghao Wei, Conor McArdle, and Prince M. Anandarajah are with the Photonics Systems and Sensing Lab (PSSL), School of Electronic Engineering, Dublin City University, 9 Dublin, Ireland (e-mail: minghao.wei2@mail.dcu.ie; conor.mcardle@dcu.ie; prince.anandarajah@dcu.ie).

Aleksandra Kaszubowska-Anandarajah is with the CONNECT Research Centre, Electronic and Electrical Engineering, School of Engineering, Trinity College Dublin, D02 W272 Dublin, Ireland (e-mail: anandara@tcd.ie).

This article has supplementary material provided by the authors and color versions of one or more figures available at https://doi.org/10.1109/JLT.2025.3567158.

Digital Object Identifier 10.1109/JLT.2025.3567158

I. INTRODUCTION

IBER Bragg Gratings (FBGs) have become indispensable in the field of optical fiber sensing due to their inherent advantages, such as high sensitivity, immunity to electromagnetic interference, multiplexing capabilities, and compact size [1], [2].

Femtosecond-laser (fs) - inscribed FBGs have gained attention for their improved robustness and temperature tolerance compared to conventional UV-written gratings [3], [4]. By enabling direct point-by-point inscription in standard fibers, fs-laser technology can fabricate ultra-weak or specialized FBG arrays that maintain stable reflection profiles under demanding conditions. Accurate interrogation of these FBGs is crucial for precise measurements [5]. Traditional interrogation techniques include tunable laser source and photodiode, broadband source and optical spectrum analyzer (OSA), edge filtering, and tunable filtering. However, they often face limitations in resolution, speed, and dynamic range, especially for static strain sensing due to laser frequency noise, spectral resolution of OSA (typically ~ 0.05 nm), intensity noise, and long integration times [6], [7], [8], [9], [10]. More recently, Optical Frequency Combs (OFCs) have been applied to FBG interrogation, serving as high-resolution spectral sources that potentially enable simultaneous interrogation of multiple FBG sensors with improved resolution [10].

OFCs are light sources with a spectrum consisting of discrete, equally spaced lines [11]. A Dual Optical Frequency Comb (DOFC) extends this concept by leveraging the interference of two OFCs with slightly different line spacing (free spectral ranges, FSRs). When the two OFCs are combined and detected by a photodetector, their optical frequencies are down-converted to radio frequencies (RF) while retaining the combs' spectral information. This heterodyne detection process generates an RF comb in which each beat note corresponds to a specific optical frequency difference between the original combs. In the field of FBG interrogation, the DOFC technique offers several advantages, such as i) high resolution and accuracy due to narrow beat linewidths in electrical spectra (down to few Hz); ii) stable frequencies of the comb lines for precise detection of frequency/wavelength shifts; iii) fast acquisition speed due to simultaneous measurement of all comb lines for dynamic sensing; iv) high dynamic range (>1000 $\mu\epsilon$) [12]; v) simple low-speed electronics vi) simplified system architecture for lack of moving parts enhancing robustness and stability.

DOFCs are generated using various techniques such as mode-locked lasers, electro-optic modulators, and gain-switching lasers [6], [10], [12], [13], [14], [15]. Among these approaches, mode-locked laser combs provide ultra-short pulses and high coherence but can be complex and costly; electro-optic combs use phase and intensity modulators offering flexibility but suffer from insertion loss and limited bandwidth.

On the other hand, gain-switched laser combs are generated by modulating the driving current of semiconductor lasers that are commercially available, generating flexible combs with simpler setups [16], [17]. Externally injected Gain-Switched Lasers (EI-GSL) present a novel solution to generating mutually coherent DOFCs [17]. In this approach, two semiconductor lasers are gain-switched at slightly different frequencies and are externally injected with light from a common semiconductor tunable laser source. This configuration ensures: i) mutual phase coherence due to external injection locking, which is crucial for stable and accurate heterodyne detection; ii) improved stability as a common injection source mitigates environmental perturbations such as temperature fluctuations and mechanical vibrations; iii) scalability for multiplexing multiple FBG sensors by generating a spectrally flat and broad OFCs that provides distinct, stable spectral channels for each sensor with minimal reconfiguration; iv) simplicity and cost-effectiveness and v) possibility for monolithic integration vi) flexibility stemming from FSR and wavelength tunability.

Various implementations of DOFC interrogation for FBGs have been reported, each with unique approaches and limitations. For instance, Guo et al. utilized a DOFC system with free-running fiber lasers to multiplex static FBG strain sensors with FWHM of 0.07 nm, dynamic range of 520 $\mu\varepsilon$ and strain resolution of 0.5 $\mu\varepsilon$ [13]. Though the approach is effective, the fiber-based laser cavity is susceptible to environmental perturbations, often requiring costly stabilization techniques or long averaging times to maintain sufficient coherence and mitigate drift. Posada-Román et al. employed electro-optic modulators to generate dual combs for fast FBG (FWHM - 200 pm) interrogation [14]. However, the complexity of the modulation setup and the need for high-frequency electronics can pose significant challenges. Kuse et al. demonstrated high-resolution strain sensing using mode-locked lasers in a DOFC setup using FBG with FWHM of 500MHz (\sim 1.78 pm) at 290.4THz [10]. The system achieved exceptional performance with a strain resolution of 34 n ε over an optical bandwidth of 1 THz by leveraging a phase-locking mechanism using free-continuous wave lasers. While highly effective, the setup requires additional feedback loops, dedicated stabilization electronics, and active control mechanisms, such as pump current modulation which can contribute to system complexity and the need for precise instrumentation.

Collectively, these approaches were used to monitor exceptionally narrow bandwidth FBGs in the range 0.0018-0.2nm with uniform spectral profiles [6], [10], [12], [13], [18]. Despite these latest advancements, challenges remain in achieving mutual

coherence between the combs, with a simplified economical setup for practical applications and using it for interrogating broadband FBGs (bandwidth ~0.5nm) with non-uniform spectral profiles. Indeed, while much effort has been devoted to optimizing the DOFC generation, the use of very narrow bandwidth FBGs is a limiting factor. Most commercial FBGs are fabricated with fs-laser processing that typically tend to have larger bandwidths than other FBGs and are usually used with high reflectivities to increase the signal-to-noise ratio. With high reflectivity and wide bandwidth FBGs, some benefits of DOFC interrogation systems, like higher resolution, cannot be directly exploited for straightforward FBG peak tracking. In that case, processing algorithms applied to the obtained spectra can improve the overall system performance and are required to obtain results at least comparable to commercial interrogators.

In this study, we investigate the interrogation of commonly used fs-written FBG with non-uniform broader profiles (bandwidths up to \sim 0.5nm) using a DOFC system generated by EI-GSL. We demonstrate that they can be monitored with comparable accuracy to the narrow bandwidth FBGs.

By refining and optimizing signal processing techniques for both reflection (hyperbolic tangent fitting, spline fitting with constant power monitoring, and FFT-based Gaussian fitting) and transmission spectra (spline fitting-based cross-correlation and inverted Gaussian fitting), we achieve high-resolution strain measurements $(0.32~\mu\varepsilon)$ with FBG shift fluctuations of \sim 0.8 pm at constant strain, notably improving upon the 1.7 pm fluctuations reported previously [18]. Our work demonstrates that selecting appropriate signal processing methods based on the spectral properties and applied strain values can significantly enhance the sensing performance of the DOFC, opening a path for their broader application in the field of fiber sensors.

II. EXPERIMENTAL SETUP

A. DOFC-FBG Interrogation Setup

To investigate high-sensitivity strain measurements using FBGs interrogated by DOFCs, we designed an experimental setup as illustrated in Fig. 1, where the DOFCs were generated using EI-GSL [17], which ensures mutual coherence between the OFCs. Specifically, two Fabry-Perot lasers (Pilot Photonics) were gain-switched at 1 GHz and 999.98 MHz repetition rates, resulting in an FSR difference (Δf) of 20 kHz. External injection from a semiconductor tunable laser (Pure Photonics) introduces the phase coherence between the combs, a critical aspect for accurate heterodyne detection and subsequent signal processing.

The two mutually coherent OFCs were combined using a 50:50 optical coupler and directed into the first port of an optical circulator. The circulator's second port was connected to the FBGs under test, allowing the combined OFC signal to interrogate the gratings. Reflected signals from the FBGs were routed back through the circulator's third port to a low-speed photodetector (Thorlabs PDA10CF) with a bandwidth of 150 MHz and a trans-impedance gain of 10⁴ V/A, enabling heterodyne detection of the two OFCs.

Since a suitable real-time oscilloscope was not available, the resulting electrical signal, containing the down-converted

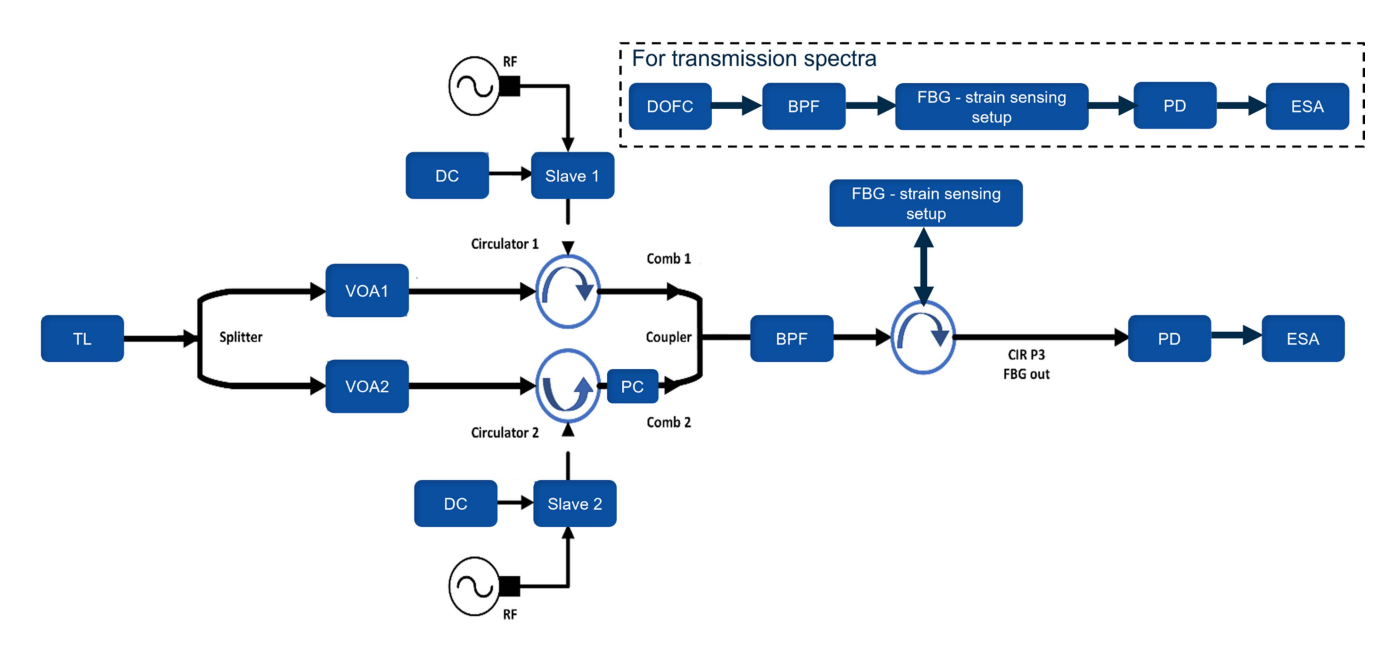


Fig. 1. Experimental setup: externally injected-gain switched laser (EI-GSL) based Dual Optical Frequency Comb (DOFC) interrogation of FBGs for static strain sensing. TL - semiconductor-based tunable laser source as seed laser, VOA - variable optical attenuator, slave – Fabry - Perot gain-switched laser, DC - power source, BPF - programmable bandpass filter, PD - photodiode, ESA - electrical spectral analyzer, PC - polarization controller. The figure in the dashed box inset is the setup used to interrogate the FBG in transmission.

RF comb with a tone spacing of 20 kHz, was analyzed using an electrical spectral analyzer (ESA - Siglent SSA3021X) at RBW of 300 Hz over a span ranging from 0.5 – 1.3 MHz. A sample comb can be seen in Fig. 2. The fs-written FBGs used for the experiments were centered at 1551.38 nm with a 0.5 nm bandwidth. Fig. 3 shows the reflection and transmission spectra of FBG acquired with an Optical Spectrum Analyzer (Thorlabs – OSA 203C). Fig. S1 depicts the injection wavelength (1551.28 nm) of the tunable laser source with reference to FBG spectra. The FBGs were mounted on one end on a precision translation stage (Thorlabs - MAX313D/M - 3-Axis NanoMax Stage) for easy pre-straining, while the other end was affixed to a piezoelectric transducer (PZT) controlled by PZT-servo controller (PI E-501 modular piezo controller). The distance between the fixed ends was ~ 30 cm. The PZT-induced strain was incremented by applying displacements ranging from 10 nm to 5 μ m, corresponding to strain variations from approximately 33.33 n ε to 32.68 $\mu\varepsilon$. This configuration facilitated the systematic assessment of the system's sensitivity and linearity over a wide range of strain values.

B. Strain Measurement and Calibration Procedure

Calibration and sensitivity measurements involved systematically applying known strain increments to the FBGs by using the PZT (PI – P-753) and recording the corresponding spectral responses. The PZT induced controlled strain increments by applying displacements of 10 μ m, 5 μ m, 1 μ m, 500 nm, 100 nm, 50 nm, and 10 nm, corresponding to strain variations of 32.68 μ e, 18.18 μ e, 3.33 μ e, 1.67 μ e, 0.33 μ e, 0.17 μ e, 33.33 ne respectively.

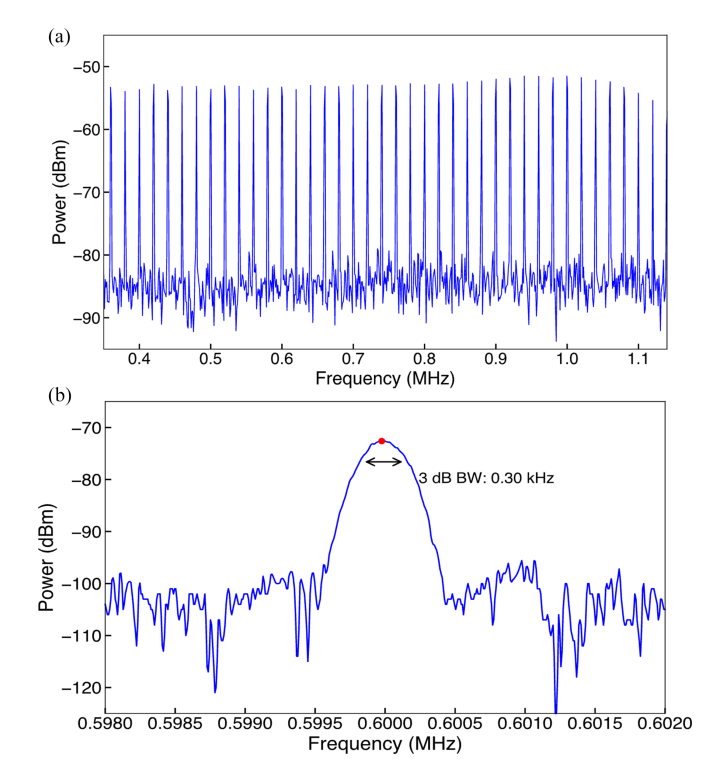


Fig. 2. (a) A sample reference RF comb having an optical 3 dB bandwidth of 0.5 nm and SNR $\sim 32 \text{ dB}$; (b) a single RF peak with a line width of 312.17 Hz, acquired from the ESA with a resolution bandwidth (RBW) of 300 Hz. Please note that (b) is a separate high-resolution measurement of a selected RF peak.

Reflection and transmission spectra were acquired using an ESA as a single shot measurement with an acquisition time of \sim 3 s, limited only by the resolution bandwidth (RBW)

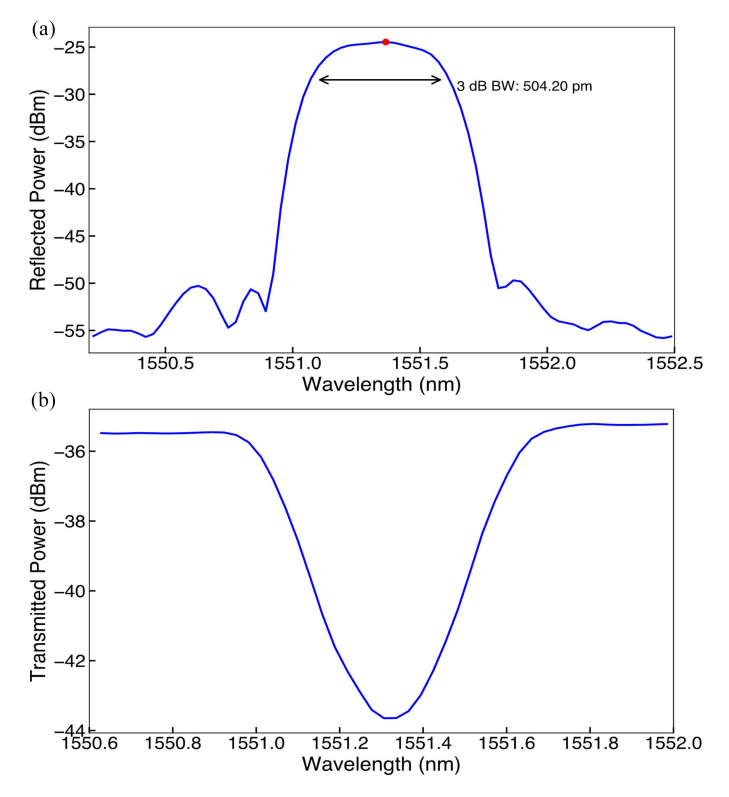


Fig. 3. Optical (a) reflection and (b) transmission spectra of a fs-written FBG with a bandwidth of 0.5nm, centered at 1551.38 nm.

of 300 Hz of the ESA. The Power Spectral Density (PSD) spectra were then processed using the following techniques for each strain step. Calibration curves were generated by plotting the extracted spectral parameters - such as inflection points from hyperbolic tangent fitting, frequencies at constant power from spline tracking, augmentations in central power from Fast Fourier Transform (FFT) analysis, and shifts of central wavelengths from the observed dips using inverted Gaussian fitting against the applied strain values. A linear fitting (linear regression analysis) was done on these data, yielding the slope, which corresponds to FBG's sensitivity. To validate the performance of the DOFC interrogation system, the FBGs were also interrogated using a commercial state-of-the-art interrogator (SmartFiber SmartScan), which serves as a benchmark due to its widespread use. Calibration plots obtained from the DOFC-based method were compared with those from the commercial interrogator, which was operated at a 2.5 kHz acquisition rate, 1000 sample averaging (i.e., 2.5 Hz processing rate), and a total acquisition time of 3 s. We employed the following formulae to convert the frequency shifts obtained from signal processing back to the optical wavelength domain corresponding to the Bragg wavelengths of the FBGs:

$$f_{FBG} = f_{inj} - \left(\frac{\Delta f_{opt}}{\delta v_{RF}}\right) \delta v_{strain} \tag{1}$$

$$\lambda_{FBG} = \frac{c}{f_{FBG}} \tag{2}$$

where δv_{strain} is the frequency shift measured by our signal processing technique, which is directly induced by the applied strain, Δf_{opt} is the FSR in optical domain (1GHz), δv_{RF} is the FSR in electrical domain (20 kHz), f_{inj} is the injection frequency of the tunable laser (193.177 THz), λ_{FBG} is the FBG shift, and c is the speed of light. This allowed us to accurately determine the FBG shifts from the frequency shifts acquired from the ESA, corresponding to the applied strains. These calibration curves were utilized to determine the system's sensitivity and linearity. The relationship between the spectral shifts and the applied strain was examined to ensure consistency and repeatability across different FBG measurement techniques. The following sections will also assess sensor metrics such as dynamic range, noise characteristic, strain resolution, and comparative performance of various signal processing methods.

Although our experimental demonstration was performed under controlled laboratory conditions, the design of our DOFC system is inherently modular and robust. In our configuration, the sensitive dual-comb unit, including the slave Fabry-Perot lasers, is housed in a hermetically sealed, environmentally controlled enclosure, and the components used in the DOFC comb source are commercially available, enhancing practical reliability. Since our FBG sensors operate in the C-band (around 1550 nm), the stable DOFC unit can be located remotely and connected via standard optical patch cords to sensors deployed in harsh or variable environments. This architecture effectively isolates the delicate components from high temperatures, extreme humidity, and vibrations, while allowing the FBG sensors to experience and report real-world conditions. Furthermore, the use of polarization-maintaining fibers within the dual-comb enclosure ensures stable optical path lengths, preserving coherence against environmental disturbances. The relatively high optical power injected from the seed laser provides a wide injection-locking range, counteracting wavelength drift in the gain-switched laser and maintaining mutual comb coherence. This robustness was previously demonstrated in a similar EI-GSL-based DOFC setup employed for gas spectroscopy [17], which exhibited excellent long-term wavelength and power stability over 60 minutes despite significant ambient perturbations typical of real-world laboratory environments.

III. THEORY AND METHODOLOGY

In this section, we present robust signal processing methodologies for accurately extracting strain-induced wavelength shifts from DOFC-interrogated FBG signals. The mutual coherence of the OFCs and the preservation of the spectral characteristics through down conversion allow for a detailed analysis of the reflected and transmitted spectra.

Our choice of signal processing algorithms was guided by both the physical attributes of the reflected and transmitted FBG spectra and practical considerations such as the 3 dB bandwidth of the optical combs. In reflection-mode analysis, we monitored the steep edges of the FBG reflection profile rather than the central peak, due to the limited 3 dB bandwidth of our optical comb. Tracking these transitions still provided a reliable marker for FBG shift, even within the restricted spectral range. First, the

hyperbolic tangent fitting was used in reflection mode because the FBG reflectivity profile (r) can often be approximated by $r = \tanh^2(\kappa L)$, where κ is coupling coefficient and L is length of grating. The inflection point provides a convenient metric for tracking the FBG's Bragg shift. This method proved especially accurate at moderate-to-higher strain increments (e.g., $>3 \mu\varepsilon$), where the reflection spectrum exhibits well-defined transitions. Second, spline fitting with a constant-power threshold provides a smooth interpolation of the reflection spectrum, reducing noise while pinpointing the frequency (or wavelength) at a chosen power level. This approach is effective in reflection mode because the FBG's transitions remain sharply defined under strain, offering a stable reference for tracking small spectral shifts without relying on the peak maximum. Third, FFT-based Gaussian fitting was introduced to capture subtle power redistribution within the ESA-acquired PSD data. While the FFT axis itself is not a straightforward physical frequency scale (owing to the lack of phase information), this approach isolates the main peak in the transformed spectrum and is particularly advantageous at finer strain levels, where minute shifts manifest as distinct changes in power of the fitted Gaussian center. For transmission-mode measurements, we applied spline fitting followed by cross-correlation to measure dips in the transmitted spectrum. This technique is traditionally effective when the spectral feature (e.g., an absorption or notch) shifts in wavelength. Cross-correlation of the spline-fitted spectra with a reference enhances peak detection even under mild noise. Additionally, since the transmission dip resembled an inverted Gaussian, we approximated the FBG's dip by an inverted Gaussian. Around the initial minimum, we selected \sim 23 data points, performed a local interpolation, and then fitted an inverted-Gaussian-like function. Even without a strictly uniform profile, this method achieved high R² at lower strain increments, as the sharp dip center was well-captured by the approximate shape. Each algorithm thus addresses a distinct aspect of the FBG's spectral response. Hyperbolic tangent fitting excels at moderate strains where a steep reflection slope exists; spline-based constant-power monitoring targets finer shifts with increased interpolation overhead; FFTbased Gaussian fitting captures small redistributions of power in the reflection spectrum; cross-correlation suits broader or multiple dips in transmission mode; and inverted Gaussian fitting can isolate broader and narrower transmission dips. Together, these methods enable robust strain tracking across a wide range of operating conditions, leveraging the dual optical frequency comb's bandwidth while accommodating diverse FBG profiles.

The following sections detail how these methods process the spectral data to improve strain-measurement precision.

A. Reflection Spectra Processing

1) Hyperbolic Tangent Fitting: Reflection spectra of the strained FBG were characterized by fitting their peaks with a hyperbolic tangent function, as described by the following equation

$$f(x) = a + b \tanh(c(x - d)) \tag{3}$$

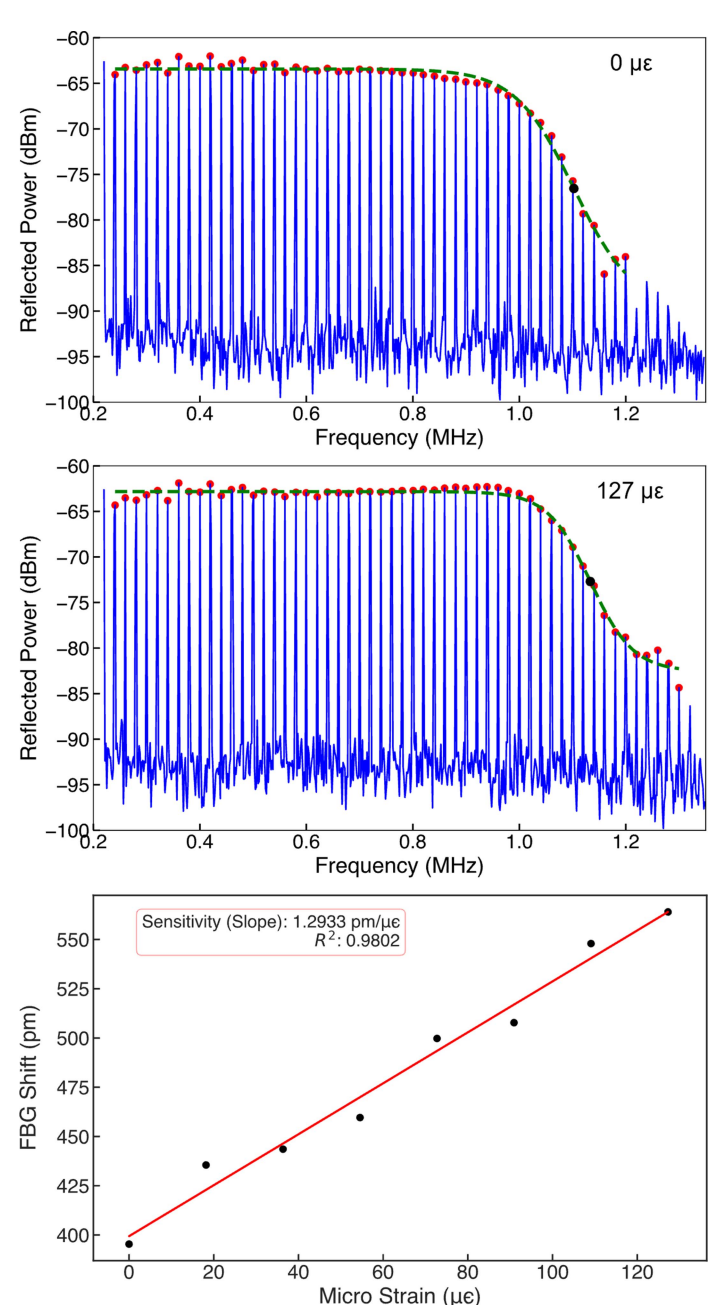


Fig. 4. Sample hyperbolic tangent fitting over reflected RF comb lines at a) pre-strained condition $(0\mu\varepsilon)$ and b) \sim 127 $\mu\varepsilon$ c) corresponding calibration plot with strain increments of 18.18 $\mu\varepsilon$. In a) and b) comb data peaks are shown (red dots), inflection point (black dot), and tanh fitting (green dash line).

where a represents the baseline power level, b represents the amplitude of transition, c controls the steepness of transition, and d identifies the central frequency at which the transition occurs. The hyperbolic tangent function effectively models the steep slope near the edges of the FBG spectra and the inflection point $(\max|f'(x)|)$ of the fitted curve, effectively tracking the spectral position of FBG shift. Fig. 4(a)–(b) depicts a sample hyperbolic tangent fittings over RF comb lines of reflected spectra of FBGs under 0 $\mu\varepsilon$ and 127 $\mu\varepsilon$ while monitoring Bragg wavelength shift by tracking the inflection point of the curves. Applying this

method, we were able to obtain a sensitivity of 1.293 pm/ $\mu\epsilon$ and an R² = 0.980 for applied strain increments of 18.18 $\mu\epsilon$, as depicted in Fig. 4(c). Fig. S2 further illustrates shifts in inflection point with applied strain in the range of 0–127 $\mu\epsilon$.

2) Spline Fitting and Constant Power Monitoring: To enhance the resolution of frequency measurements, a univariate spline fitting procedure was applied to the RF comb lines, as expressed by the equation:

$$s(f) = \sum_{i=0}^{N} c_i \cdot B_i(f)$$
 (4)

where $B_i(f)$ is the basis of the spline functions, and c_i is the coefficient determined through the fitting process. The spline interpolation smooths the noise fluctuations or discretization errors in the peaks, producing a continuous curve that accurately represents the underlying spectral profile. Detailed comparisons regarding the resolution improvements achieved by this method, relative to alternative approaches, are presented in the Results section.

To track the position of the FBG under different strains, we adopted the frequency coordinates as reference at which the fitted splines intercept a threshold set at a specific power level of $-66 \, \mathrm{dBm}$ - a value empirically optimized to maximize linearity and maintain a high signal-to-noise ratio.

Fig. 5(a)–(b) shows the spline fitting curve over the RF comb lines for two strains (0 $\mu\varepsilon$ and 53 $\mu\varepsilon$) applied to the FBG. Fig. S3 further illustrates this procedure by demonstrating the shift in frequencies at a constant power threshold (i.e., -66 dBm). Specifically, for applied strain increments of 3.33 $\mu\varepsilon$ for strains ranging from 0–53 $\mu\varepsilon$. In Fig. 5(c), we demonstrate the corresponding calibration curve with the sensitivity of 0.774 pm/ $\mu\varepsilon$ with $R^2=0.976$.

3) Fast Fourier Transform and Gaussian Curve Fitting: In this approach, the PSD data obtained from the ESA was processed using the Fast Fourier Transform (FFT) to reveal a power distribution that is characteristic of each strained FBG, as shown in Fig. 6(a). A Gaussian curve was fitted using (5) over the FFT data to monitor the central peak and quantify the increased power as a function of applied strain, as depicted by Fig. 6(a).

The x-axis produced here does not represent a direct physical RF frequency in MHz, so we label it as 'arbitrary units'.

$$f(x) = a \exp\left(-\frac{(x-c)^2}{2d^2}\right) + e$$
 (5)

where a is the amplitude, c is the center frequency, d is the standard deviation and e accounts for any baseline offset.

During the fitting, zero-frequency peak components, corresponding to uninformative DC components, were removed, and the Gaussian fitting was applied to the remaining peaks, which denotes actual power redistribution due to strain-induced FBG shifts. As strain is applied to the FBG, we observed an increase in the power of the central peak at zero frequency in the FFT-transformed data (Fig. 6(b) and Fig. S4). Indeed, a substantial portion of the comb gets transmitted as the Bragg wavelength shifts to higher wavelengths with increasing strain. By tracking the increment in the amplitude of the central Gaussian peak, we

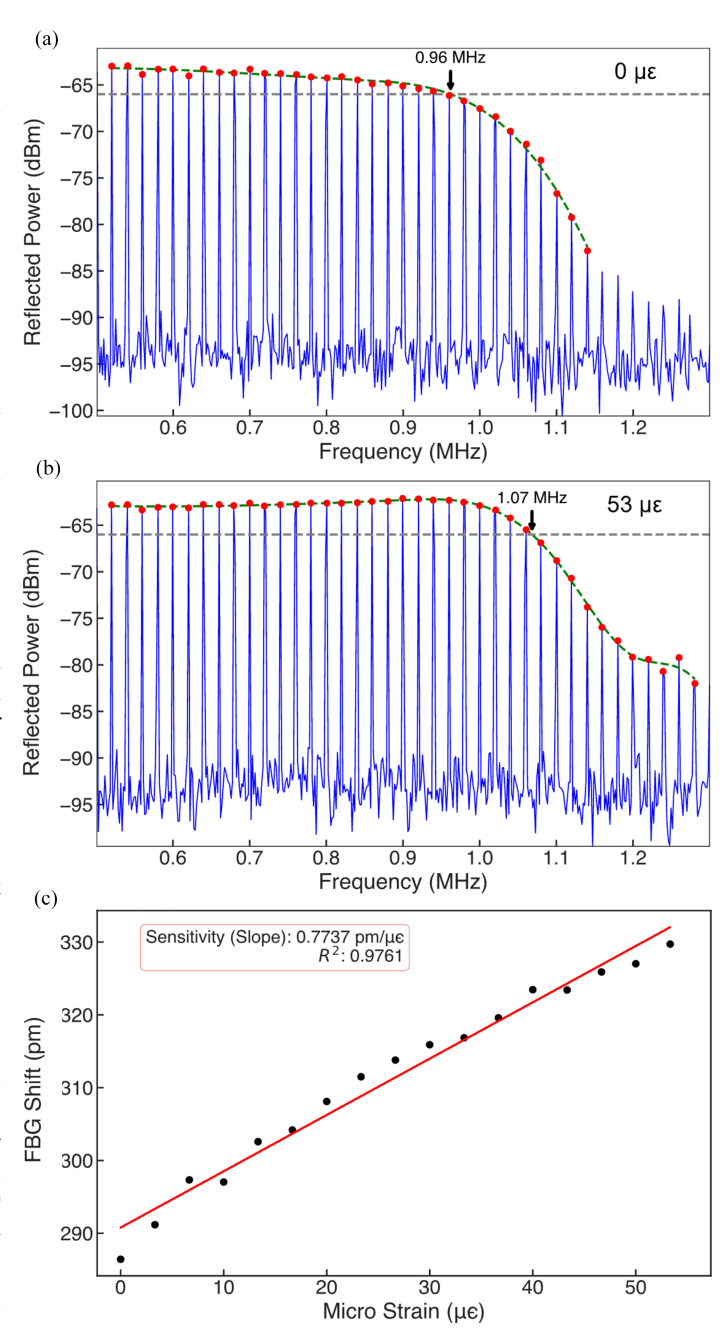


Fig. 5. Spline fitting over reflected RF comb lines at a) pre-strained condition $(0 \, \mu \varepsilon)$ and b) $\sim 53 \, \mu \varepsilon$ c) corresponding calibration plot with strain increments of 3.33 $\mu \varepsilon$. Red markers denote the peaks of the RF comb data, the dotted green line represents spline fitting, and the dashed grey line represents a constant power reference at $-66 \, \mathrm{dBm}$.

could correlate the changes directly to strain-induced modifications in the FBG's reflection spectrum. Applying this method, we were able to obtain a sensitivity of 0.0210 dBm/ $\mu\varepsilon$ and an R² = 0.986 for strain increments of 3.33 $\mu\varepsilon$ in the range of 0 $\mu\varepsilon$ -53 $\mu\varepsilon$.

B. Transmission Spectra Processing

The transmission spectrum was obtained by removing the circulator (C3) from the experimental setup and connecting the

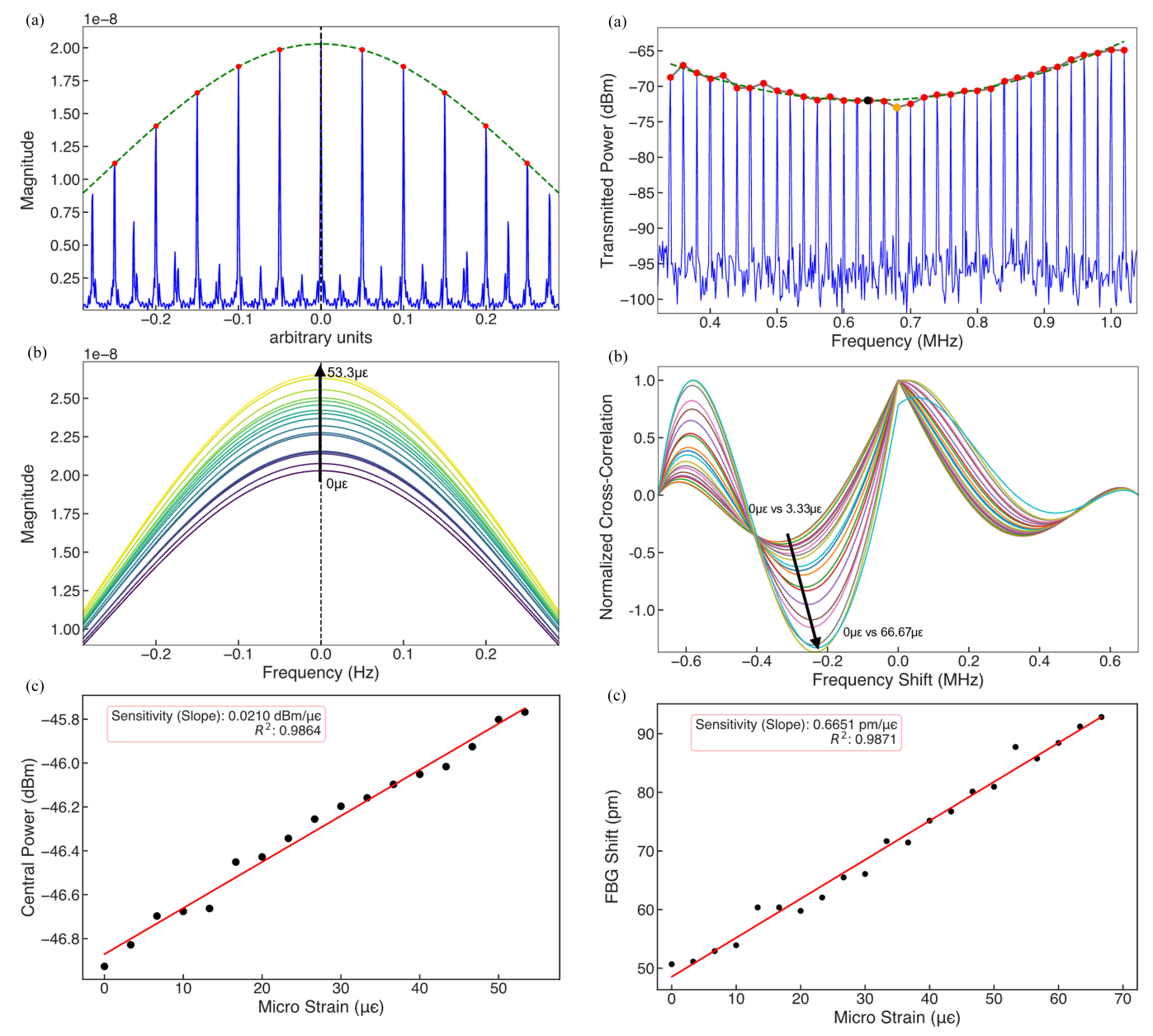


Fig. 6. (a) Gaussian fitting over reflected FFT data, (b) combined Gaussian fitted curves at various strains (0 $\mu\varepsilon$ – 53 $\mu\varepsilon$) in steps of 3.33 $\mu\varepsilon$ with a clear increment in FFT magnitude at the central frequency, (c) corresponding calibration plot. In a), red dots represent FFT peaks used for Gaussian fitting (green line), and the dotted black line indicates the reference f=0 for power measurements.

Fig. 7. (a) Spline fitting over transmitted RF combs acquired via ESA at RBW of 300 Hz, (b) combined plot of cross-correlation functions corresponding to various strains (0 $\mu\varepsilon$ – 67 $\mu\varepsilon$) with strain increment step size of 3.33 $\mu\varepsilon$ (spline fitting over 0 $\mu\varepsilon$ data is considered as reference), c) corresponding sensitivity/calibration plot. Red markers denote the peaks of the RF comb, orange marker denotes the initial dip (before fitting), and black marker denotes the actual dip (after fitting).

other end of the FBG directly to the photodiode (see inset Fig. 1). The acquired RF spectra were then processed using the following methods tailored to capture the distinct features of the comb transmitted through the gratings.

1) Spline Fitting Followed by Cross-Correlation: The transmission spectra for all standard fs-written FBGs were initially processed using spline fitting over RF comb lines acquired from ESA to create smooth, continuous representations of the spectral data. Cross-correlation analysis was performed between the reference (pre-strained) spectrum and the spectra obtained under various incremental strain conditions, as described by

(6). The lag at which the cross-correlation function reached its minimum indicated the relative shift between the spectra and was monitored accordingly, as depicted in Fig. 7.

The reference spectrum (at nominal zero strain) and the strained FBG spectra were fitted, and their cross-correlation was calculated according to the formula:

$$F(\varphi) = \int_{-\infty}^{\infty} X(f) \cdot Y(f + \varphi) df$$
 (6)

where X(f) and Y(f) are the reference and current spectral profiles, respectively and φ is frequency lag (MHz). Applying this method, we were able to obtain a sensitivity of 0.665 pm/ $\mu\varepsilon$ and an R² = 0.987 for strain increments of 3.33 $\mu\varepsilon$ in the range of 0 $\mu\varepsilon$ – 67 $\mu\varepsilon$.

2) Inverted Gaussian Fitting: In the transmission spectra, distinct attenuation features manifested as dips corresponding to the Bragg wavelengths, were observed in the RF spectra. To precisely quantify the central wavelength shifts induced by varying micro-strains, each spectral dip was modeled using an inverted Gaussian function, using (7), as depicted in Fig. 8.

$$f(x) = a - b \cdot \exp\left(-\frac{(x-c)^2}{2d^2}\right)$$
 (7)

where a is the baseline power level, b is the amplitude of the dip, c is the central frequency of the dip and d is the standard deviation of the dip. Applying this method, we were able to obtain a sensitivity of 0.684 pm/ $\mu\varepsilon$ and an R² = 0.995 for strain increments of 3.33 $\mu\varepsilon$ in the range of 0 $\mu\varepsilon$ – 67 $\mu\varepsilon$.

To assess the computational overhead of our signal processing algorithms, we evaluated their execution time for processing a single CSV file (with typical data sizes of several hundred to a few thousand points) over 10 runs on our system - an AMD Ryzen 5 5600U (2.30 GHz) with 16 GB RAM, running Windows 11 Pro 64-bit and Python 3.11.7 (packaged by Anaconda). Our measurements show that the hyperbolic tangent fitting routine requires an average of 15.98 ms per file, while the spline fitting with constant-power monitoring and the spline fitting with crosscorrelation methods take approximately 11.07 ms and 14.56 ms, respectively. In contrast, the FFT-based Gaussian fitting method executes in about 10.59 ms on average, and the inverted Gaussian fitting method, owing to its additional interpolation and more complex fitting process, averages around 118.63 ms per file. Despite the longer processing time of the inverted Gaussian approach, all methods complete in under 120 ms per file, which is well within acceptable limits for near real-time operation on a modest desktop system. Table SI summarizes the average execution times and corresponding standard deviations for the various processing algorithms.

This quantitative comparison confirms that our chosen algorithms are computationally efficient, balancing speed and the complexity required to capture subtle spectral features.

IV. RESULTS AND DISCUSSION

For all the signal processing techniques described above, the sensitivity was determined by plotting the measured spectral shifts against the applied strain increments, as described in the experimental setup section. The calibration plots exhibited sensitivities in the range 0.7-1.1 pm/ $\mu\varepsilon$ in good agreement with the theoretical expectation for standard silica FBGs (\sim 1.2 pm/ $\mu\varepsilon$) [1] and comparable to the performance of the commercial interrogator. The observed slight differences in sensitivity can be attributed to the inherent characteristics of each technique and the spectral properties of the FBGs used. Strain sensitivity measurements were done using various signal processing techniques for strain increments in the range 33 n ε -3.3 $\mu\varepsilon$, as detailed

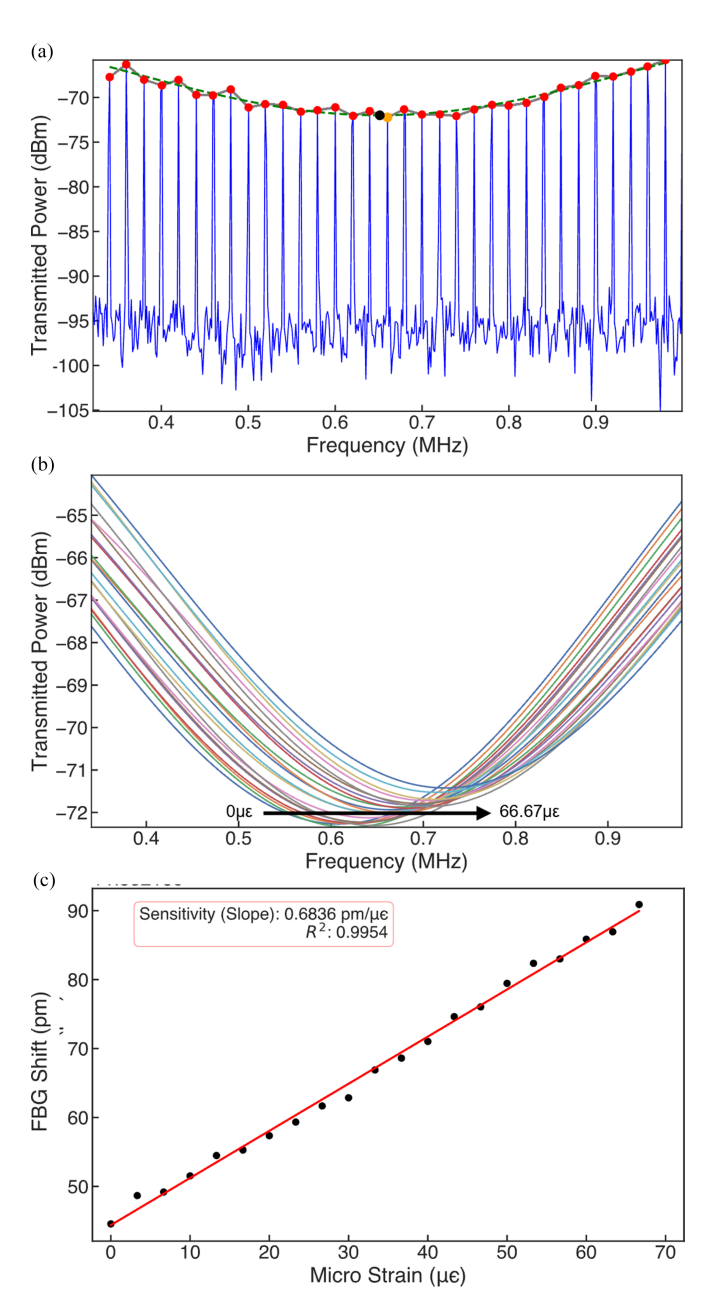


Fig. 8. (a) Inverted Gaussian fit over a FBG RF comb spectrum, (b) combined Gaussian fitted curves corresponding to various strains (0 $\mu\epsilon$ – 67 $\mu\epsilon$) with strain increment step of 3.33 $\mu\epsilon$, (c) corresponding sensitivity/calibration plot. Red markers denote the peaks of the RF comb data, orange marker denotes the initial dip - before fitting, and black marker denotes the actual dip - after fitting.

in the experimental section. For clarity, we present here the detailed calibration curves and sensor metrics for only the two extreme values of strain increment $(33 \text{ n}\varepsilon \text{ and } 3.33 \mu\varepsilon)$ out of the broader set analyzed, leaving the full set of data to Fig S5. These increments were selected to exemplify the key differences in sensor performance metrics among various methods. The relative calibration curves for various processing methods are reported in Fig. 9, where the left column of the plots corresponds to a strain increment of $3.33 \mu\varepsilon$, while the right column shows the data obtained for strain increments of $33 \text{ n}\varepsilon$. From top to bottom, the rows display data analyzed using spline and FFT-Gaussian fitting

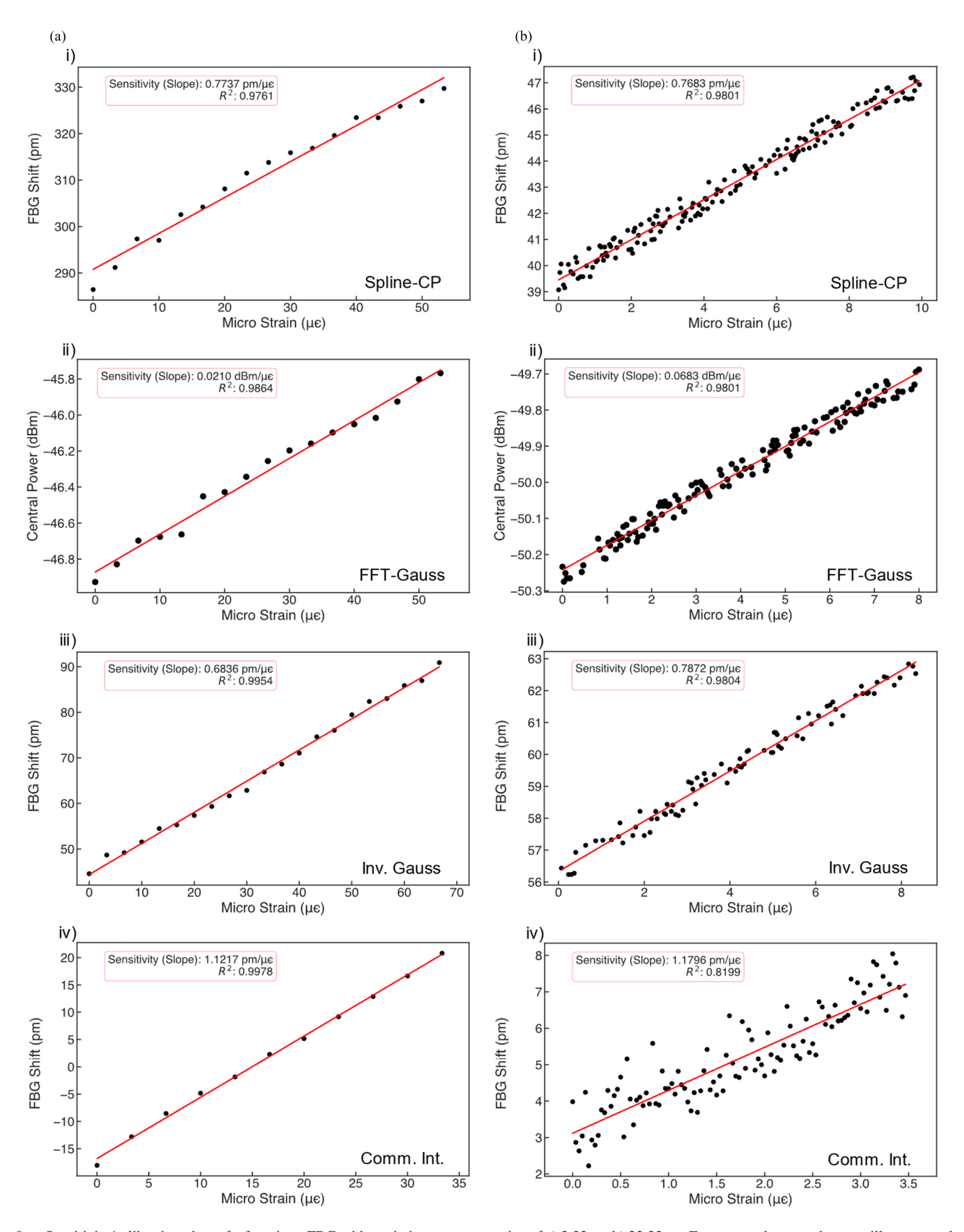


Fig. 9. Sensitivity/calibration plots of a fs-written FBG with strain increment step size of a) $3.33~\mu\varepsilon$ b) $33.33~n\varepsilon$. From top to bottom, the rows illustrate analysis methods applied to: (i) reflection spectra using spline fitting (Spline-CP) and (ii) FFT-Gaussian fitting (FFT-Gauss), (iii) transmission spectra using the inverted Gaussian fitting method (Inv. Gauss), and (iv) measurements obtained from a state-of-the-art commercial interrogator (Comm. Int.) with 1000 averaging, data processing rate of 2.5Hz, and an integration time of 3~s.

on reflection spectra, inverted Gaussian fitting on transmission spectra, and measurements obtained from a commercial interrogator, respectively. Fig. S5 compares various sensitivity plots with applied strain increments of 33.33 n ε , 0.17 $\mu\varepsilon$, 0.33 $\mu\varepsilon$, 1.67 $\mu\varepsilon$ and 3.33 $\mu\varepsilon$, for inverted Gaussian fitting (for transmitted FBG data), spline fitting and constant power monitoring (for reflected FBG data) and commercial interrogator methodologies.

The system's linearity was evaluated by examining the calibration curves over the range of applied strains. At lower PZT displacements, corresponding to smaller strain increments (33.33 n ε -0.33 $\mu\varepsilon$), the FBGs interrogated using the DOFC demonstrated superior linearity with $R^2 > 0.97$ compared to the commercial interrogator ($R^2 \sim 0.82$), especially for strain increment of 33 n ε , 166 n ε , and 333 n ε (R² values of 0.82, 0.94 and 0.96 respectively), as seen in Fig. 9 and Fig. S5. This enhanced linearity at low strains was attributed to the mutual coherence of the combs in the DOFC system and signal processing techniques, enabling precise strain measurements. The commercial interrogator exhibited better linearity at relatively higher strain increments (>3.33 $\mu\varepsilon$). This observation suggests that while the DOFC system excels in detecting minute strain variations, its performance is constrained at higher strain levels due to the limitations in the 3 dB bandwidth (62 GHz) and spectral flatness of the DOFC spectral output. Similarly, even the dynamic range limit, 422 $\mu\varepsilon$, of the DOFC interrogation system can be attributed to limitations in 3dB bandwidth and spectral flatness. The comb's flatness ensures uniform power distribution across the comb lines, which is essential for maintaining consistent sensitivity throughout the measurement range. Beyond this dynamic range, the reduced overlap between the comb lines and the FBG reflection spectrum reduces the sensitivity and accuracy of the system.

The noise performance was assessed by measuring power fluctuations of the ESA spectrum over a period of 5 s with the FBG in unstrained condition ($\varepsilon=0$). The observed fluctuations were found to be less than $\sim\!0.32$ dB, as seen in Fig. S6, indicating a stable and relatively low-noise system operation. Power fluctuations near 0 Hz were excluded since they do not correspond to the FBG strain-induced signal and are likely introduced by instrument-related effects. This low level of noise and an SNR of $\sim\!32$ dB, as observed with the ESA, contribute to the repeatability and reliability of the strain measurements.

The mutual coherence of the dual-comb along with the robustness of the signal processing algorithms, enhances the immunity of the system to noise and external disturbances.

For FBGs operated in reflection mode, the hyperbolic tangent fitting method effectively measured strains down to 3 $\mu\varepsilon$. However, spline fitting with frequency monitoring at constant power levels and FFT with Gaussian fitting demonstrated superior performance at lower strains (sub- $\mu\varepsilon$). Whereas for the interrogation of FBGs in transmission mode, spline fitting with cross-correlation proved effective for strains exceeding 3 $\mu\varepsilon$. For lower strain values, the inverted Gaussian fitting method provided enhanced sensitivity, enabling accurate monitoring even for broad bandwidth fs-written FBGs with non-uniform spectral profiles. To ascertain the standard deviation of the measurements under each signal processing algorithm, we monitor

the signal under pre-strained conditions at nominal strain $\varepsilon =$ 0. Measurements were acquired for a duration of 120 s at a constant strain level below the detection threshold to establish the baseline noise characteristics of the system. The average power and the corresponding standard deviation were calculated for each signal processing method (Fig. S7). The standard deviation derived from these analyses served as an empirical estimate of the noise floor of the system. The minimum FBG fluctuations were found to be ~ 0.8 pm (Table I – spline fitting and constant power monitoring). Subsequently, we compared the standard deviations obtained from the calibration plots by analyzing the residuals of the linear fit (σ_c) - where the system's response to known strain increments was characterized by those obtained under pre-strained conditions ($\sigma_{\rm p}$). To unify the noise metrics, we defined Σ as the maximum of the standard deviations obtained from both the calibration plots and the pre-strained condition measurements, as shown in (8). This comparative analysis ensures consistency and validates the reliability of the sensor performance across different operational scenarios. Furthermore, the effective strain resolution (Res) for strain increments of \sim 33 n ε was determined by dividing the standard deviation obtained from calibration plots (σ_c) by the sensitivity (S), as seen in (9):

$$\Sigma = \max \left(\sigma_c, \sigma_p \right) \tag{8}$$

$$Res = \sigma_c / S \tag{9}$$

Under this criterion, the minimum strain resolution was found to be $\sim 0.32~\mu\varepsilon$ (see Table I), with uncertainty of $\pm 0.003~\mu\varepsilon$ due to repeatability constraint from the linear actuator used in the experiment.

To evaluate the performance of various signal processing algorithms used for monitoring FBG shifts, we defined a Figure of Merit (FoM) as the ratio of the sensitivity (S – pm/ $\mu\varepsilon$) or dBm/ $\mu\varepsilon$) to the maximum standard deviation (Σ) as follows:

$$FoM = S/\Sigma \tag{10}$$

This metric provides a normalized assessment of each method's efficacy, enabling a direct comparison of their performance in detecting ultra-fine strains, where higher FoM values indicate better performance. Table I summarizes this comprehensive analysis for applied strain increments of 33 n ε . In Fig. 10, we also illustrate graphically the comparison between the FoM presented in Table I. The FFT-Gaussian fitting and spline-constant power monitoring methods consistently achieved higher FoMs, suggesting enhanced sensitivity to minute strain variations. Also, the spline-CP algorithm has a FoM slightly higher than the commercial interrogator. Extending the same analysis for larger increments (see Fig. 11 and Fig. S8), we registered that, at strain increments exceeding 0.33 $\mu\varepsilon$, the commercial interrogator demonstrated a higher FoM than the other signal processing techniques, indicating better performance. In contrast, for increments below 0.33 $\mu\varepsilon$, the FFT-Gaussian fitting and spline-constant power monitoring methods consistently achieved higher FoMs (see Fig. 11).

This reduction in linearity and Figure of Merit (FoM) at higher strains mainly stems from the limited ~0.5 nm 3 dB bandwidth

| TABLE I |
|---|
| COMPREHENSIVE ANALYSIS OF VARIOUS METHODOLOGIES USED ALONG WITH SENSOR METRICS (STANDARD DEVIATIONS AND SENSITIVITY) TO DETERMINE |
| FIGURE OF MERIT (FOM) AND RESOLUTION |

| Method | $\sigma_{ m c}$ | $\sigma_{ m p}$ | S | Strain resolution (με) (±0.003 με) | FoM |
|---|-----------------|-----------------|----------------------------|---------------------------------------|-------|
| Hyperbolic tangent | 8.192 pm | 1.016 pm | - | 0 | 0 |
| Spline Fitting and constant power monitoring | 0.319 pm | 0.835 pm | 0.768 pm/με | 0.415 | 0.920 |
| Fast Fourier Transform and Gaussian Curve Fitting | 0.0219 dBm | 0.026 dBm | $0.068 \\ dBm/\mu\epsilon$ | 0.321 | 2.582 |
| Spline Fitting - Cross- Correlation | 1.824 pm | 1.704 pm | - | 0 | 0 |
| Inverted Gaussian Fitting | 0.256 pm | 1.266 pm | 0.787 pm/με | 0.324 | 0.621 |
| Commercial interrogator | 0.564 pm | 1.341 pm | 1.179 pm/με | 0.478 | 0.879 |

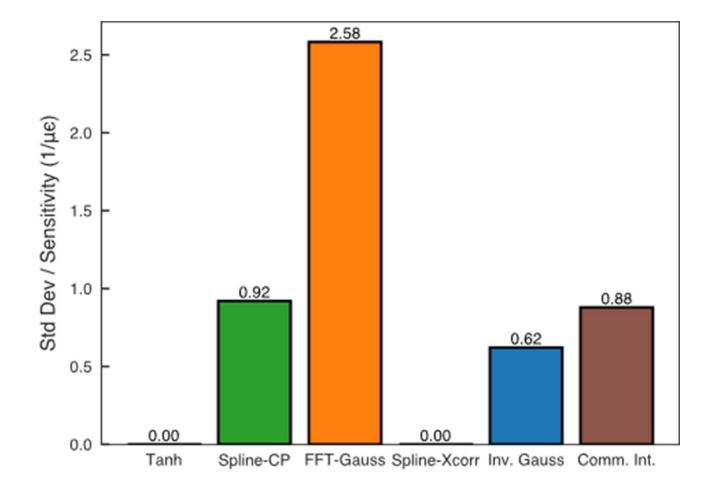


Fig. 10. Plot of Figure of Merit (sensitivity/std deviation, $1/\mu\epsilon$) vs. various fitting methods for strain increments of 33 n ϵ over an integration time of 120 s. Tanh – hyperbolic tangent, Spline-CP - spline fitting and monitoring frequencies at constant power, FFT-Gauss - FFT and Gaussian fitting, Spline-Xcorr - spline fitting followed by cross-correlation, Inv. Gauss – inverted Gaussian fitting, Comm. Int - commercial interrogator.

shared by both the comb and the FBG, causing the reflection peak to leave the comb's flatter region and thus lowering R². To mitigate this, several spectral optimization methods could be employed. Comb spectral flatness and bandwidth can be enhanced via electro-optic modulators [19], fibre-based [15] or semiconductor optical amplifier (SOA)-based [20] nonlinear broadening schemes, or through comb-flattening filters. Alternatively, shifting the injection wavelength (see Fig. S1) offers a cost-effective solution, though it may slightly degrade the optical carrier-to-noise ratio. Furthermore, dynamic range can be significantly improved by appropriately engineering the FBG profile. Broadband gratings can accommodate larger wavelength shifts within the comb's flat region, while very narrowband or cascaded narrowband gratings can be selected such that their

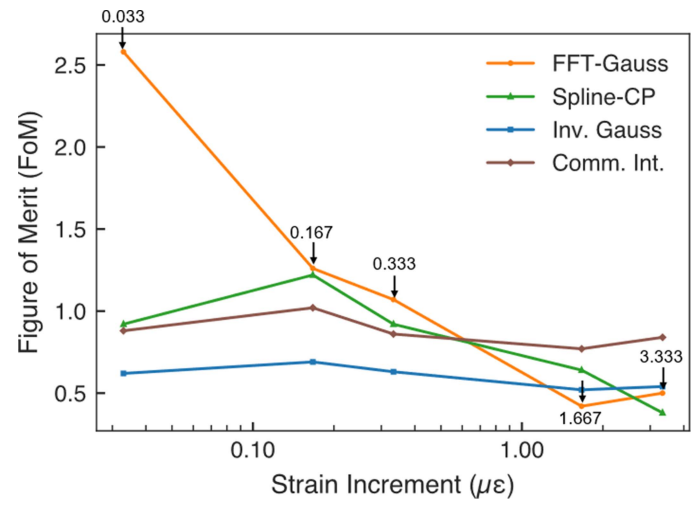


Fig. 11. Figure of merit vs strain increments for different signal processing methods.

reflection or transmission spectra consistently remain within the comb's uniform bandwidth.

Future efforts will explore these approaches to simplify operation and extend the dynamic strain range without frequent system adjustments. However, at small strain increments ($< 0.33~\mu\varepsilon$), the DOFC spectra of FBG can be processed with different algorithms to obtain elevated FoM and sub-microstrain strain resolution. This fact underscores the potential of the proposed signal processing techniques in achieving precise and reliable strain measurements, even for fs-written FBGs with non-uniform spectral profiles. In addition, it confirms their suitability for high-resolution sensing applications, where accurate and ultra-fine strain measurements are critical.

Achieving high resolution with DOFC-based FBG interrogation critically depends on matching the spectral characteristics of the comb and the FBG. When the 3 dB bandwidth of FBG is narrow relative to the comb line spacing, only a few comb lines

sample the FBG's reflection profile, which may lead to increased uncertainty in identifying spectral shifts. Conversely, if the comb is excessively dense relative to a broad FBG response, the presence of many closely spaced lines may necessitate additional spectral smoothing to average out minor fluctuations, potentially reducing resolution. Furthermore, if the comb's flatness is suboptimal, the signal-to-noise ratio near the grating's peak degrades, further limiting resolution. Under optimal conditions, where the comb spacing and 3 dB bandwidth are well matched to that of the FBG, a higher Q factor is achieved, enabling more precise tracking of strain-induced shifts.

Although our DOFC system is optimized for static and low-frequency strain measurements, its dynamic performance is limited by the effective sampling of the down-converted RF comb signal. This effective sampling rate is dictated by the RF comb line spacing, set by the difference in the repetition rates of the gain-switched lasers and the acquisition rate of the ESA. With a typical RF spacing of 20 kHz, the Nyquist limit defines the highest dynamic strain frequency that can be resolved without aliasing. Importantly, our system allows tuning of the RF comb line spacing through adjustments in the laser drive parameters; such tuning can effectively raise the Nyquist limit, thereby improving the system's ability to capture faster strain variations. However, the limitations in terms of comb spacing might not be an issue for mechanical measures that have bandwidth typically below 1kHz.

V. CONCLUSION

We showcased the first comprehensive demonstration of DOFC-FBG interrogation techniques applied to standard fswritten gratings for high-resolution (0.32 $\mu\varepsilon$) FBG strain sensing. By optimizing signal processing techniques, specifically employing FFT – Gaussian fitting, spline fitting with frequency monitoring at constant power levels for reflection data, and inverted Gaussian fitting for transmission data, we achieved sensitivities around 1 pm/ $\mu\varepsilon$ and great linearity (R² > 0.98) at nano-strain increments (33 n ε). The system's performance for static strain sensing applications surpasses standard commercial interrogators at strain increments below 330 n ε . While limitations in dynamic range exist due to comb spectral properties, the overall findings underscore the efficacy of combining DOFC interrogation with tailored signal processing methods, which can be potentially used for real-time monitoring of static parameter variations.

The calibration and validation of the system confirm its potential for advanced sensing applications, where ultra-fine strain measurements are crucial. Future work will focus on optimizing the bandwidth and flatness of dual-comb for distributed sensing applications, exploring its capabilities in dynamic strain monitoring scenarios to further enhance the performance of the DOFC interrogation for FBGs.

REFERENCES

 M. A. Nagar, D. Janner, "Polymer-based optical guided-wave biomedical sensing: From principles to applications,", vol. 11, pp. 972, 2024, doi: 10.3390/photonics11100972

- [2] R. Correia, S. James, S.-W. Lee, S. P. Morgan, and S. Korposh, "Biomedical application of optical fibre sensors," *J. Opt.*, vol. 20, no. 7, Jun. 2018, Art. no. 073003, doi: 10.1088/2040-8986/aac68d.
- [3] B. Xu et al., "Femtosecond laser point-by-point inscription of an ultra-weak fiber Bragg grating array for distributed high-temperature sensing," *Opt. Exp.*, vol. 29, no. 20, pp. 32615–32626, Sep. 2021, doi: 10.1364/OE.437479.
- [4] J. He, B. Xu, X. Xu, C. Liao, and Y. Wang, "Review of femtosecond-laser-inscribed fiber Bragg gratings: Fabrication technologies and sensing applications," *Photon. Sens.*, vol. 11, no. 2, pp. 203–226, Jun. 2021, doi: 10.1007/s13320-021-0629-2.
- [5] D. Tosi, "Improved KLT algorithm for high-precision wavelength tracking of optical fiber Bragg grating sensors," *J. Sensors*, vol. 2017, no. 1, 2017, Art. no. 5412825, doi: 10.1155/2017/5412825.
- [6] R. Zhang, Z. Zhu, and G. Wu, "Static pure strain sensing using dual-comb spectroscopy with FBG sensors," *Opt. Exp.*, vol. 27, no. 23, pp. 34269–34283, Nov. 2019, doi: 10.1364/OE.27.034269.
- [7] M. M. M. Werneck, R. C. S. B. Allil, and F. V. B. de Nazaré, "Interrogation techniques of fiber Bragg gratings," *Fiber Bragg Gratings, Theory, Fabr., Appl.*, vol. TT114, pp. 65–77, 2017, doi: 10.1117/3. 2286558.ch6.
- [8] Q. Liu, T. Tokunaga, and Z. He, "Realization of nano static strain sensing with fiber Bragg gratings interrogated by narrow linewidth tunable lasers," *Opt. Exp.*, vol. 19, no. 21, pp. 20214–20223, Oct. 2011, doi: 10.1364/OE.19.020214.
- [9] J. Guo, S. Xue, Q. Zhao, and C. Yang, "Ultrasonic imaging of seismic physical models using a phase-shifted fiber Bragg grating," *Opt. Exp.*, vol. 22, no. 16, pp. 19573–19580, Aug. 2014, doi: 10.1364/OE.22. 019573.
- [10] N. Kuse, A. Ozawa and Y. Kobayashi, "Static FBG strain sensor with high resolution and large dynamic range by dual-comb spectroscopy,", Opt. Express, vol. 21, pp. 11141–11149, doi: 10.1364/OE.21.011141
- [11] N. R. Newbury, "Searching for applications with a fine-tooth comb," Nat. Photon., vol. 5, no. 4, pp. 186–188, Apr. 2011, doi: 10.1038/ nphoton.2011.38.
- [12] K. Zhao, H. Jia, P. Wang, J. Guo, X. Xiao, and C. Yang, "Free-running dual-comb fiber laser mode-locked by nonlinear multimode interference," *Opt. Lett.*, vol. 44, no. 17, pp. 4323–4326, Sep. 2019, doi: 10.1364/OL.44.004323.
- [13] J. Guo, Y. Ding, X. Xiao, L. Kong, and C. Yang, "Multiplexed static FBG strain sensors by dual-comb spectroscopy with a free running fiber laser," *Opt. Exp.*, vol. 26, no. 13, pp. 16147–16154, Jun. 2018, doi: 10.1364/OE.26.016147.
- [14] J. E. Posada-Roman, J. A. Garcia-Souto, D. A. Poiana, and P. Acedo, "Fast interrogation of fiber Bragg gratings with electro-optical dual optical frequency combs," *Sensors*, vol. 16, no. 12, p. 12, Dec. 2016, doi: 10.3390/s16122007.
- [15] P. M. Anandarajah et al., "Generation of coherent multicarrier signals by gain switching of discrete mode lasers," *IEEE Photon. J.*, vol. 3, no. 1, pp. 112–122, Feb. 2011, doi: 10.1109/JPHOT.2011.2105861.
- [16] P. D. Lakshmijayasimha, P. M. Anandarajah, P. Landais, and A. Kaszubowska-Anandarajah, "Optical frequency comb expansion using mutually injection-locked gain-switched lasers," *Appl. Sci.*, vol. 11, no. 15, p. 15, Jan. 2021, doi: 10.3390/app11157108.
- [17] E. P. Martin, S. T. Ahmad, S. Chandran, A. Rosado, A. A. Ruth, and P. M. Anandarajah, "Stability characterisation and application of mutually injection locked gain switched optical frequency combs for dual comb spectroscopy," *J. Lightw. Technol.*, vol. 41, no. 13, pp. 4516–4521, Jul. 2023.
- [18] X. Zhao, Q. Li, S. Yin, J. Chen, and Z. Zheng, "Dual-comb dynamic interrogation of fiber Bragg grating with one mode-locked fiber laser," *IEEE Sensors J.*, vol. 18, no. 16, pp. 6621–6626, Aug. 2018, doi: 10.1109/JSEN.2018.2852846.
- [19] R. Zhou, S. Latkowski, J. O'Carroll, R. Phelan, L. P. Barry, and P. Anandarajah, "40nm wavelength tunable gain-switched optical comb source," *Opt. Exp.*, vol. 19, no. 26, pp. B415–B420, Dec. 2011, doi: 10.1364/OE.19.00B415.
- [20] P. D. Lakshmijayasimha, A. Kaszubowska-Anandarajah, E. P. Martin, P. Landais, and P. M. Anandarajah, "Expansion and phase correlation of a wavelength tunable gain-switched optical frequency comb," *Opt. Exp.*, vol. 27, no. 12, pp. 16560–16570, Jun. 2019, doi: 10.1364/OE.27.016560.